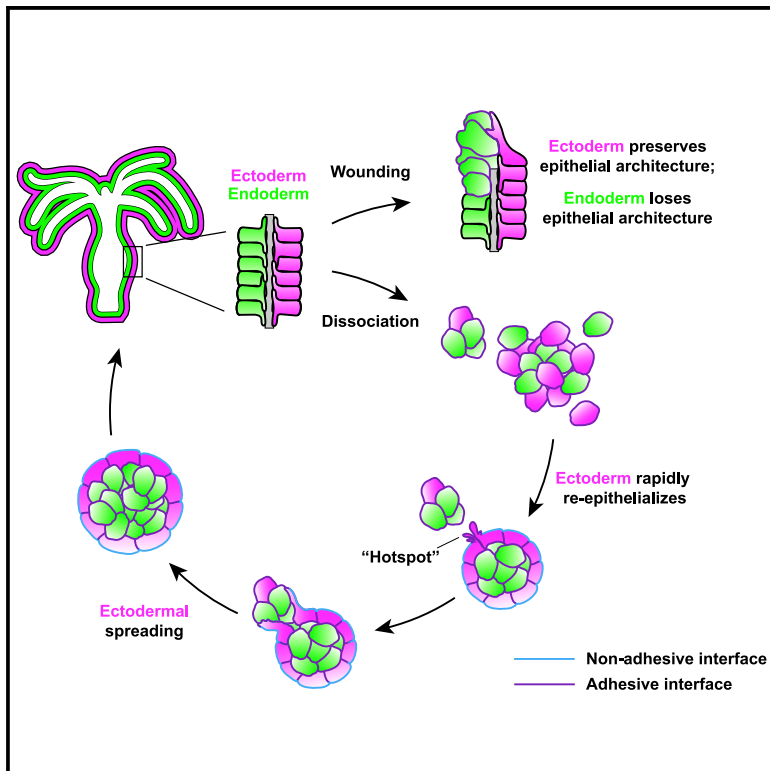


Current Biology

Cell Sorting in *Hydra vulgaris* Arises from Differing Capacities for Epithelialization between Cell Types

Graphical Abstract



Authors

Taylor D. Skokan, Ronald D. Vale,
Kara L. McKinley

Correspondence

valer@janelia.hhmi.org (R.D.V.),
kara_mckinley@fas.harvard.edu (K.L.M.)

In Brief

Skokan et al. dissect the cellular behaviors underlying cell sorting in *Hydra*. Cells that rapidly restore an epithelial monolayer adopt exterior positions by engulfing non-epithelialized aggregates and single cells. Similar responses to local damage suggest common mechanisms for restoring compartmentalization in wound healing and self-organization.

Highlights

- All cell lineages can sort to the interior of ectodermal aggregates
- Reaggregated ectodermal cells reform an epithelium; endodermal aggregates do not
- The ectodermal epithelium engulfs cells and aggregates adhered to its surface
- Local wounding elicits sorting-associated cell behaviors

Article

Cell Sorting in *Hydra vulgaris* Arises from Differing Capacities for Epithelialization between Cell Types

Taylor D. Skokan,¹ Ronald D. Vale,^{1,2,3,*} and Kara L. McKinley^{1,*}

¹Howard Hughes Medical Institute and Department of Cellular and Molecular Pharmacology, University of California, San Francisco, San Francisco, CA 94158, USA

²Howard Hughes Medical Institute Janelia Research Campus, Ashburn, VA 20147, USA

³Lead Contact

*Correspondence: valer@janelia.hhmi.org (R.D.V.), kara_mckinley@fas.harvard.edu (K.L.M.)

<https://doi.org/10.1016/j.cub.2020.07.035>

SUMMARY

Hydra vulgaris exhibits a remarkable capacity to reassemble its body plan from a disordered aggregate of cells. Reassembly begins by sorting two epithelial cell types, endoderm and ectoderm, into inner and outer layers, respectively. The cellular features and behaviors that distinguish ectodermal and endodermal lineages to drive sorting have not been fully elucidated. To dissect this process, we use micromanipulation to position single cells of diverse lineages on the surface of defined multicellular aggregates and monitor sorting outcomes by live imaging. Although sorting has previously been attributed to intrinsic differences between the epithelial lineages, we find that single cells of all lineages sort to the interior of ectodermal aggregates, including single ectodermal cells. This reveals that cells of the same lineage can adopt opposing positions when sorting as individuals or a collective. Ectodermal cell collectives adopt their position at the aggregate exterior by rapidly reforming an epithelium that engulfs cells adhered to its surface through a collective spreading behavior. In contrast, aggregated endodermal cells persistently lose epithelial features. These non-epithelialized aggregates, like isolated cells of all lineages, are adherent passengers for engulfment by the ectodermal epithelium. We find that collective spreading of the ectoderm and persistent de-epithelialization in the endoderm also arise during local wounding in *Hydra*, suggesting that *Hydra*'s wound-healing and self-organization capabilities may employ similar mechanisms. Together, our data suggest that differing propensities for epithelialization can sort cell types into distinct compartments to build and restore complex tissue architecture.

INTRODUCTION

Defining the mechanisms that organize cells into distinct compartments in the body is critical for understanding development and regeneration and has facilitated the development of synthetic models of complex biological tissues and structures [1]. Pioneering work by Townes and Holtfreter showed that dissociated cells from the amphibian embryo spontaneously sort from one another when recombined, reforming distinct layers reminiscent of their native organization [2]. Mechanistic dissection of this sorting phenomenon can provide fundamental insights into how cellular properties give rise to tissue organization across diverse systems.

Previous studies in a variety of experimental models point to cell-intrinsic differences as crucial drivers of cell sorting (reviewed in [3]). In particular, differences in adhesion strength or biophysical properties between cell types can affect sorting outcomes, lending support to models like the differential adhesion hypothesis (DAH) and differential interfacial tension hypothesis (DITH) [4–9]. These models broadly attribute sorting to differences among cell types that affect the areas of cell contacts until

energetically favorable configurations are achieved [4, 8, 9]. In addition to the contributions of cell-intrinsic differences, cell positioning can also be affected by features of a cell's surroundings. For example, neighboring cells locally modulate cell behaviors and properties at compartment boundaries in the *Drosophila* wing disc and *Xenopus* embryo [10–12]. How cell-intrinsic and extrinsic factors intersect to govern cell position remains unclear.

The freshwater cnidarian *Hydra vulgaris* is a particularly powerful model of cellular self-organization, as *Hydra* can reassemble its entire body plan from a collection of dissociated cells within days [13]. The *Hydra* body plan is largely defined by two epithelial compartments—an inner layer termed the endoderm and an outer layer termed the ectoderm—organized as concentric monolayers separated by an extracellular matrix (Figure 1A). A third, interstitial cell lineage includes neurons, gland cells, and specialized stinging cells (nematocytes) scattered throughout the body [14]. Following dissociation and reaggregation, the endodermal and ectodermal compartments are rapidly re-established as the first major step toward rebuilding the animal [13, 15, 16]. Cell proliferation and trans-differentiation are minimal or

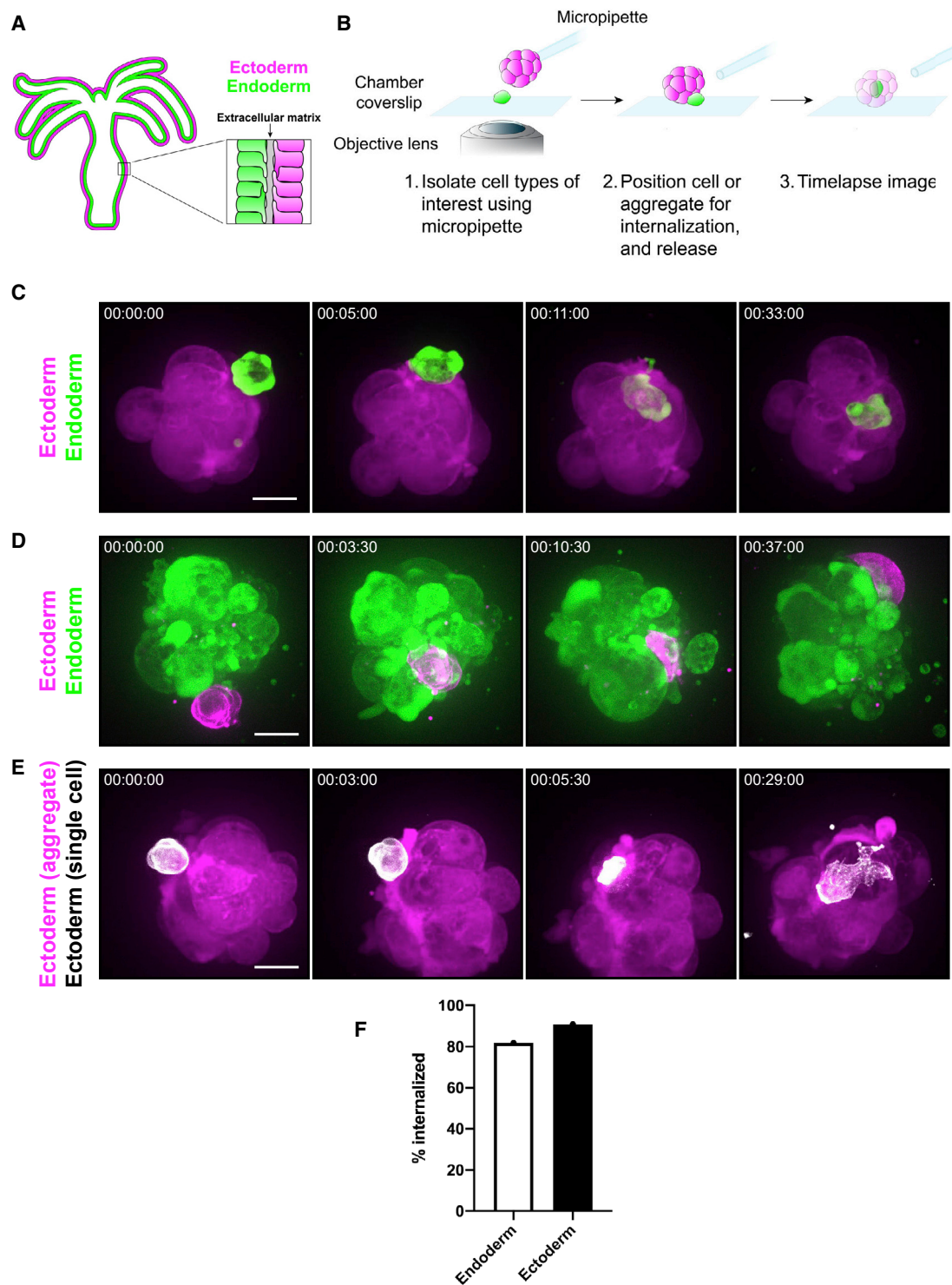


Figure 1. Ectodermal Aggregates Internalize Single Cells of Both Epithelial Cell Types

(A) Schematic of the *Hydra* body plan depicting the organization of ectodermal and endodermal lineages in concentric monolayers.

(B) Schematic of cell internalization assay using micromanipulation.

(C) Representative time course of an ectodermal aggregate expressing DsRed2 (magenta) internalizing a single endodermal cell expressing GFP (green). Quantification is shown in (F).

(D) Representative time course of an ectodermal cell expressing LifeAct-GFP (magenta) adhered to the surface of an endodermal aggregate expressing DsRed2 (green; n = 10 from 7 independent sample preparations).

(legend continued on next page)

absent during these early stages, underscoring the central role for cell sorting in rebuilding the *Hydra* body plan [13, 16]. *Hydra* represents a unique model in which rapid cell sorting gives rise to functional tissues.

In *Hydra*, cell-intrinsic differences in biophysical properties and motility have been proposed as key drivers of endodermal/ectodermal cell sorting. Specifically, endodermal and ectodermal lineages exhibit different interfacial tensions and adhesive properties largely consistent with the requirements of the DAH and DITH described above [16–19]. Differences in endodermal and ectodermal cell motility have also been proposed to drive sorting [20, 21]. However, attempts to track large numbers of cells during this process failed to show lineage-specific differences in the speed or directionality of migration [17, 22, 23]. Thus, despite evidence for biophysical properties contributing to sorting, previous approaches have left many unanswered questions regarding the cellular interactions underlying rapid compartmentalization in *Hydra*.

Here, we combine cellular micromanipulation and live microscopy to dissect the mechanisms of cell sorting in *Hydra*. Surprisingly, we find that single cells of all lineages, including ectodermal cells, sort to the interior of ectodermal aggregates. We find that aggregated ectodermal cells rapidly reform a polarized epithelial monolayer, which indiscriminately engulfs cells adhered to its surface by a wound-healing-like process. Cells that are unable to rapidly reform an epithelium, such as endodermal aggregates and isolated ectodermal cells, readily adhere to the ectodermal epithelium and are positioned at the aggregate interior during engulfment. Together, our data suggest that a key feature distinguishing the ectoderm and endoderm and driving their sorting is their capacity for rapid multicellular organization. We find that differences in the maintenance and restoration of epithelial organization between the ectoderm and endoderm arise during both self-organization and local wound healing, suggesting that common mechanisms may underlie regeneration at cellular and organismal scales. Overall, our data support a model in which cell sorting can be driven by differences in re-epithelialization among distinct cell populations.

RESULTS

Ectodermal Aggregates Internalize Diverse *Hydra* Cell Types, Including Isolated Ectodermal Cells

The predominant models for cell sorting in *Hydra* propose that intrinsic differences in the properties of endodermal and ectodermal cells direct them to sort into interior and exterior compartments, respectively. We sought to directly test this role for cell identity in directing sorting, as well as to identify cellular behaviors that may not be reflected in existing models. To this end, we first developed a method that rendered the sorting process amenable to physical manipulation and high-resolution

microscopy. Historically, sorting in *Hydra* has been analyzed by combining dissociated cells by centrifugation, which generates aggregates approximately 300–800 μm in diameter or larger [13, 15–17, 24]. These aggregate preparation methods preclude study of the initial minutes of sorting, restrict physical control over the process, and generate limited cellular and subcellular resolution due to light scattering. Therefore, we developed an approach that allowed us to isolate aggregates of relatively small sizes to facilitate high-resolution imaging (approximately 60 μm ; [Figure S1A](#); [STAR Methods](#)). We combined this method with a microscope-mounted micropipette aspirator to allow us to initiate interactions between specific lineages at precisely defined positions ([Figure 1B](#)).

As a proof of principle, we first tested how ectodermal aggregates expressing a lineage-specific DsRed2 interacted with single GFP-expressing endodermal cells. As expected, isolated endodermal cells placed in contact with the surface of ectodermal aggregates were rapidly internalized and subsequently remained at the aggregate interior ([Figures 1C](#) and [S1B](#); [Video S1A](#)). In contrast, ectodermal cells placed in contact with endodermal aggregates were not internalized; instead, ectodermal cells adhered to and spread over the endoderm, as previously described for single cells and larger aggregates [20, 21] ([Figure 1D](#); [Video S1B](#)). Thus, this micromanipulation approach facilitates controlled induction of cell sorting.

We employed our assay to directly test the role of cell identity in determining cell positioning by manually combining cells and aggregates of specific lineages ([Figure 1B](#)). To this end, we placed DsRed2-expressing ectodermal aggregates in contact with GFP-expressing cells of all *Hydra* lineages, including interstitial stem cells, neurons, nematocytes, and ectodermal epithelial cells. We found that all cell types placed in contact with ectodermal aggregates were efficiently internalized and, like endodermal cells, remained within the aggregate for the duration of our experiments ([Figures 1E](#), [S1C](#), and [S1D](#); [Videos S1C–S1F](#)). Most surprisingly, ectodermal aggregates even internalized isolated ectodermal cells at high frequency ([Figures 1E](#) and [1F](#); [Video S1C](#)). Thus, the ectoderm can robustly internalize a wide array of *Hydra* cell types, including cells of its own lineage, revealing that (1) cell sorting in *Hydra* does not depend on unique features of the endodermal lineage and (2) the same lineage can experience opposing sorting outcomes when present as single cells as opposed to multicellular aggregates. Together, these findings demonstrate that cell lineage alone cannot be the determinant of whether cells adopt inner or outer positions during sorting.

Differences in Epithelialization Generate Distinct Adhesive Properties between and within Lineages

As ectodermal aggregates internalized all cells independently of their identity, we sought to determine what distinguishes the

(E) Representative time course of an ectodermal aggregate expressing DsRed2 (magenta) internalizing a single ectodermal cell expressing LifeAct-GFP (white). Quantification is shown in (F).

(C–E) All frames depict maximum intensity projections of 50-to-100- μm z stacks. Timestamps, hh:mm:ss. Scale bars, 20 μm . See also [Video S1](#).

(F) Quantification of the frequency at which single endodermal cells or single ectodermal cells were internalized by ectodermal aggregates (endoderm: $n = 11$ from 5 independent sample preparations; ectoderm: $n = 11$ from 10 independent sample preparations). Note that, for these experiments, all cells were positioned in contact with hotspots on ectodermal aggregates, as characterized in [Figure 2](#).

See also [Figure S1](#).

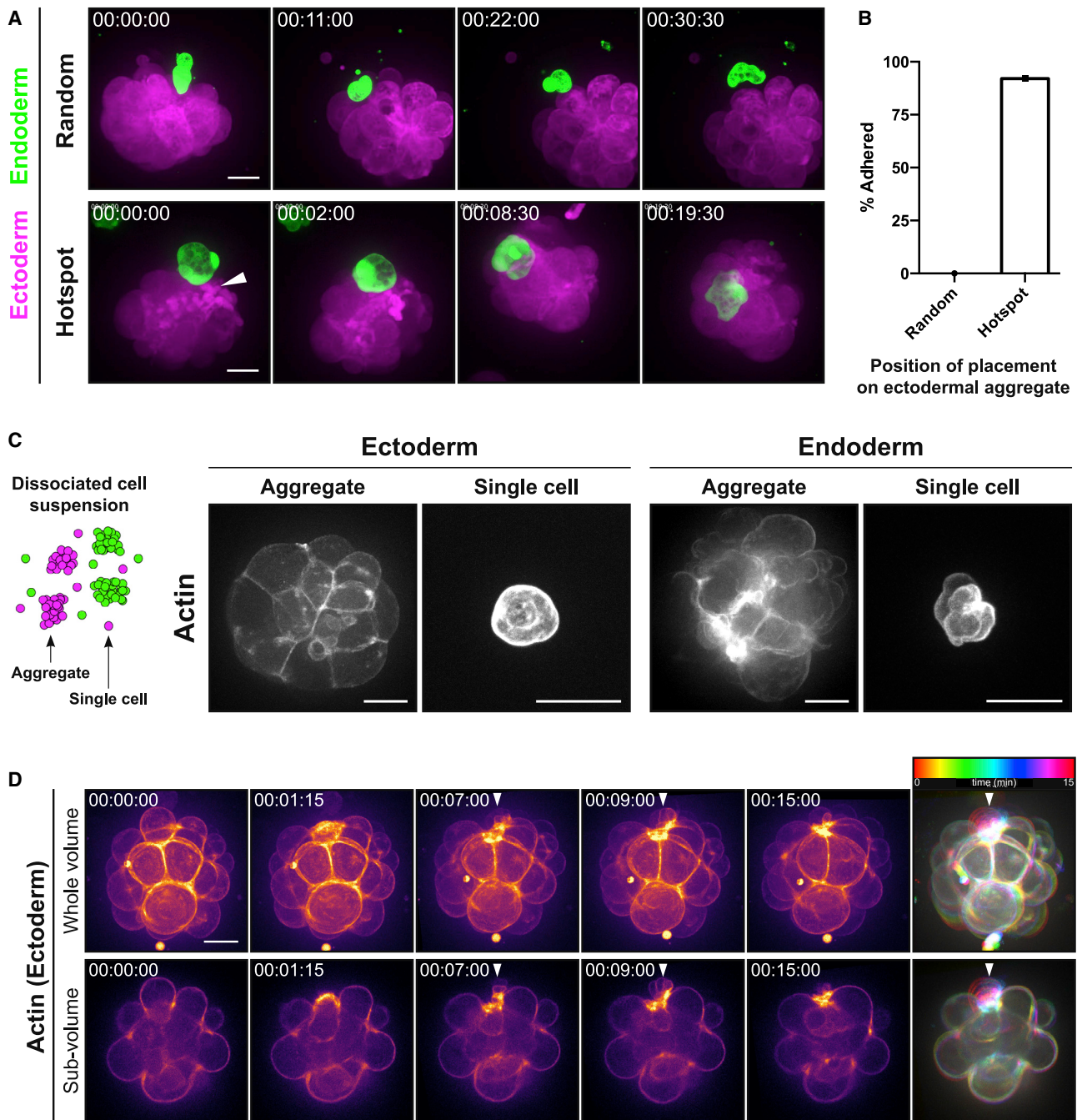


Figure 2. Ectodermal Aggregates and Internalized Entities Differ in Adhesive Properties and Multicellular Organization

(A) Representative time courses of ectodermal aggregates expressing DsRed2 (magenta) placed in contact with isolated endodermal cells expressing GFP (green) at either random positions (top) or at hotspots (bottom). Arrowhead denotes hotspot. Due to a lack of adhesion following random placement, aggregates were repeatedly repositioned via micropipette to remain in contact with the endodermal cell.

(B) Quantification of the frequency of successful adhesion between ectodermal aggregates and endodermal cells within 15 min of placement at either random positions or at hotspots on the ectodermal aggregate surface (random: $n = 12$ from 4 independent sample preparations; hotspot: $n = 12$ from 5 independent sample preparations). These experiments were performed in parallel with internalization experiments in Figure 1, such that hotspot data here include the endodermal internalization data graphed in Figure 1F.

(C) Left: schematic depicting the structures present in dissociated cell suspensions. Right: representative stills of actin organization in aggregates or single cells expressing LifeAct-GFP ($n \geq 10$ for all entities depicted). See also Video S2.

(D) Time course of hotspot formation as a result of epithelial remodeling in a small ectodermal aggregate expressing LifeAct-GFP. Arrowhead denotes a hotspot forming at a site of cell ingress. Bottom panels depict an optical section from the same aggregate. mpl-inferno LUT (FIJI) was applied to aid in visualizing graded LifeAct-GFP signal. Temporal color-coded time series (right) depicts actin organization and dynamics in the same aggregate. Hotspot (arrowhead) (legend continued on next page)

ectodermal aggregate from the entities that it internalizes. During the development of the micromanipulation assay, we found that endodermal and ectodermal cells and aggregates exhibited striking differences in their capacity to establish stable contacts with other cells. The ectodermal aggregate was broadly unable to adhere to cells placed in contact with its surface (Figures 2A and 2B). Instead, adhesion and subsequent internalization were restricted to morphologically distinct sites on the aggregate surface, which we term “hotspots” (Figures 2A, 2B, and S2A). These sites could be identified prior to manipulation by the presence of local membrane ruffling (Figure 2A). Positioning cells in contact with these pre-identified sites was predictive of successful internalization (Figure 2B). In contrast to the ectodermal aggregates, the entire surface of endodermal aggregates readily adhered when placed in contact with other cells (Figure 1D). Importantly, both single endodermal cells and single ectodermal cells were also adherent (Figures 1C–1E). Together, these findings reveal that all entities that are internalized exhibit uniform adhesion, whereas adhesion is spatially restricted in ectodermal aggregates.

The data described above demonstrated that ectodermal aggregates differ from both endodermal aggregates and, crucially, single ectodermal cells in their adhesive properties and the positions they adopt during sorting. To determine what gives rise to these differences, we compared aggregates and single cells of the ectodermal and endodermal lineages expressing LifeAct-GFP or myosin regulatory light chain-GFP (MRLC-GFP). Actomyosin localization functions as a reporter of tissue organization and polarity by labeling apical cell junctions in both the endoderm and ectoderm in intact *Hydra* [25, 26], as in other epithelial tissues [27]. Although LifeAct expression has been reported to affect actin in some systems [28, 29], prior characterization in *Hydra* reported LifeAct localization consistent with endogenous actin organization at cell junctions and no defects in major developmental or physiological processes [25]. Single cells of both epithelial lineages exhibited diffuse cortical actin localization (Figure 2C; Video S2), as expected for isolated cells in suspension [30]. Similar actin localization was observed in endodermal aggregates (Figure 2C; Video S2). Endodermal aggregates and isolated cells of both epithelial lineages also exhibited constitutive membrane blebbing (Figure S2B; Video S2), consistent with endodermal “pseudopods” previously suggested to drive sorting [21]. However, inhibiting endodermal blebbing with the myosin II inhibitor (S)-nitro-blebbistatin had no discernible effect on internalization, suggesting that this behavior is nonessential for sorting (Figures S2C and S2D; Video S3). The disordered and dynamic nature of the endoderm and isolated ectodermal cells contrasted starkly with the architecture of ectodermal aggregates, which retained the characteristic junctional actomyosin organization observed in intact *Hydra* epithelia, with relatively smooth and stable aggregate surfaces (Figures 2C and S3A; Video S2). Thus, the epithelial entities that are internalized share common dynamics and actin architecture, despite their differing lineages.

Notably, the adhesion-permissive “hotspots” we identified on the surface of ectodermal aggregates were marked by local disorganization of the otherwise robust junctional actomyosin network (Figures 2D and S3A). We found that hotspots arose either in response to local aggregate remodeling, for example, at sites of spontaneous cell ingression (Figure 2D; Video S4A), or where the edges of newly sheared ectodermal tissue fragments met to form spherical aggregates (Figure S3B; Video S4B). These surface irregularities were frequently resolved over time as new cell-cell contacts were formed (Figures 2D and S3B; Video S4). Altogether, these findings suggest that hotspots reflect sites of local epithelial discontinuity. Thus, in contrast to their endodermal counterparts, ectodermal aggregates maintain and restore epithelium-like architecture, which restricts cell adhesion to sites of epithelial discontinuity.

Restoration of Ectodermal Epithelial Continuity Positions Cells in Aggregate Interiors

We next sought to determine the cellular mechanisms by which ectodermal aggregates internalize cells following their adhesion to hotspots. To this end, we visualized ectodermal aggregates expressing LifeAct-GFP internalizing unlabeled endodermal aggregates. We observed a striking spreading and enveloping behavior of ectodermal cells surrounding captured endodermal aggregates. This process was characterized by the extension of dynamic, actin-rich protrusions from cells bordering sites of internalization. As the protrusive fronts of adjacent ectodermal cells met following internalization, new cell junctions formed to re-establish epithelial continuity (Figure 3A; Video S5A). The protrusive and zipper behaviors were reminiscent of epithelial wound healing reported in other systems [31, 32]. These data suggest that the ectodermal cell dynamics associated with restoring epithelial continuity drive the internalization of cells adhered to the aggregate surface.

Having identified these ectodermal cell behaviors associated with sorting in our small aggregate system, we next asked how these processes play out in large aggregates comparable to those used in previous sorting analyses (≥ 300 – $800 \mu\text{m}$ diameter) [17, 24]. We generated large aggregates containing both unlabeled endoderm and LifeAct-GFP-labeled ectoderm by centrifuging suspensions of dissociated cells and used live microscopy to visualize cells in the most superficial layers of the resulting aggregates (Figure 3B). Using this approach, we observed ectodermal cells spreading via actin-rich protrusions and gradually reintegrating into continuous epithelial patches. As with cell internalization (Figure 3A), LifeAct-GFP accumulated at cell junctions as new cell-cell contacts were established (Figure 3B; Video S5B). These findings suggest that the ectodermal behaviors underlying cell sorting in small aggregates also restore ectodermal epithelial continuity on larger length scales.

coincides with locally disrupted actin architecture and membrane blebbing. Image registration was used to correct for translation of the aggregate. Images were recorded at 15-s time points. See also Video S4.

(A–D) All frames depict maximum intensity projections of 50-to-100- μm z stacks. Timestamps, hh:mm:ss. Scale bars, 20 μm . See also Figures S2 and S3 and Video S3.

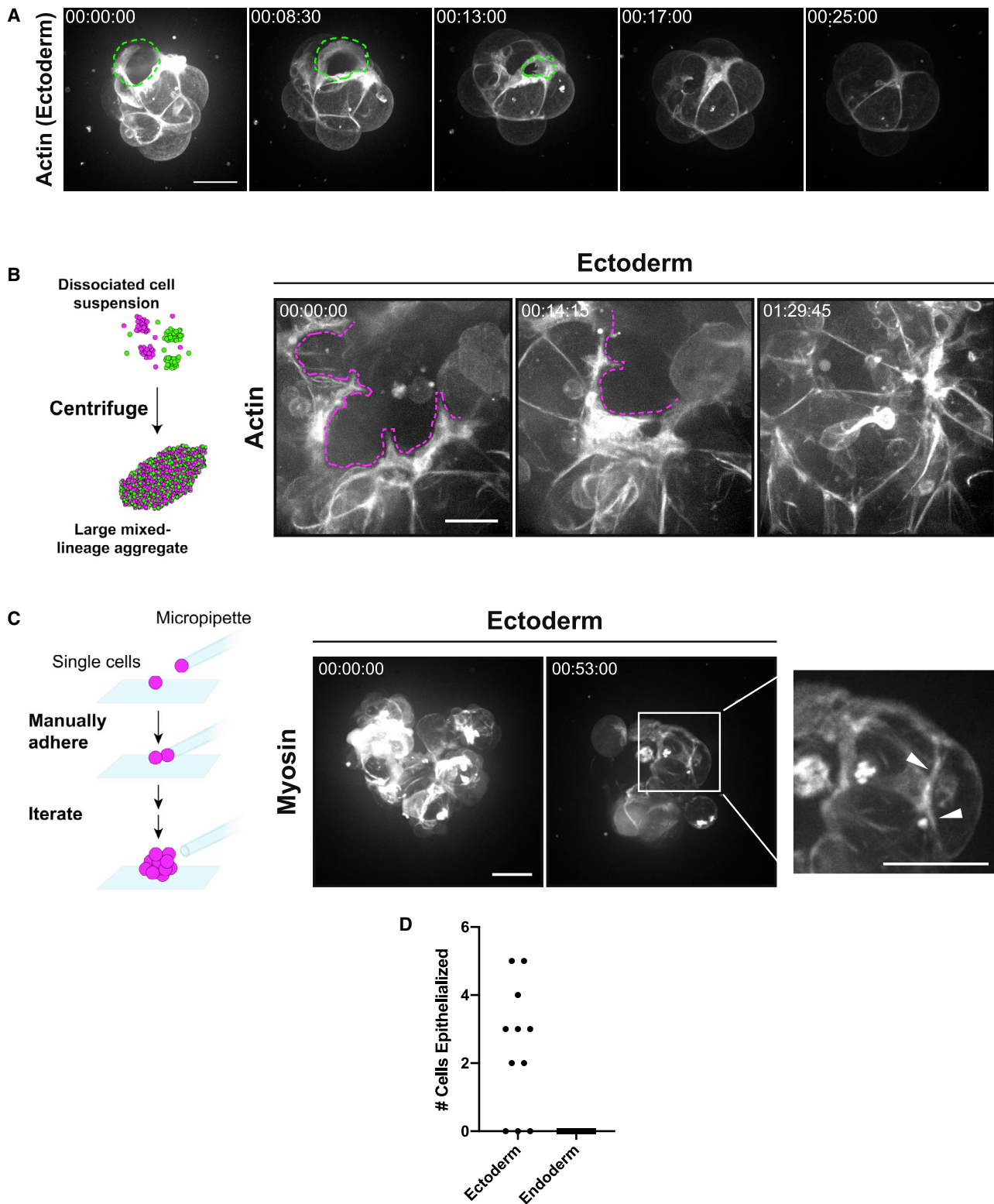


Figure 3. Ectoderm and Endoderm Differ in the Maintenance and Restoration of Epithelial Architecture

(A) Representative time course of an ectodermal aggregate expressing LifeAct-GFP internalizing an unlabeled endodermal aggregate. Dashed line indicates the position of the endodermal aggregate ($n = 20$ from 14 independent sample preparations).

(legend continued on next page)

Ectodermal Epithelial Architecture Is Rapidly Re-established following Disruption

Our observations above suggested that the conditions necessary for sorting arise as consequences of the ectoderm's propensity to maintain and locally re-establish epithelial continuity. However, both large and small aggregates exhibited some degree of ectodermal epithelial architecture at the onset of these experiments. We, therefore, directly tested whether ectodermal cells can re-establish epithelial architecture *de novo*, starting from single cells. To this end, we used micromanipulation to manually reassemble ectodermal aggregates (~40–80 μm diameter) from single cells expressing MRLC-GFP by iteratively adhering cells to one another (Figure 3C). Despite their initial lobed appearance and diffuse myosin localization, manually assembled ectodermal aggregates gradually matured into roughly spherical structures, with myosin accumulating at newly formed cell junctions (Figures 3C and 3D; Video S5C). Single endodermal cells also readily adhered to one another and could be manually reassembled into aggregates. However, we observed no indications of re-epithelialization in these aggregates (Figures 3D and S4; Video S5D), consistent with the stable, but non-epithelialized, endodermal aggregates that arise from partial dissociation (Figure 2C). These experiments confirm that the ectodermal lineage is not only predisposed to maintain and repair its epithelial architecture, but also to rapidly re-establish it following complete cellular dissociation.

Differential Maintenance of Epithelial Architecture Is Recapitulated in Local Wounding

In light of our observations that ectodermal continuity during sorting was restored through a wound-healing-like process, we considered whether the lineage-specific epithelialization behaviors that we identified contributed to the response to other forms of epithelial disruption in the animal. To this end, we analyzed the cellular response of ectodermal and endodermal tissues to wounding. We excised living fragments from the *Hydra* body column and sequentially imaged these fragments near their center, to assess the properties of the intact monolayer, and at their edges, to monitor the properties of the wound front, where tissue continuity was locally disrupted (Figure 4A). In the central regions, LifeAct-GFP localized to all cell-cell contacts in both the ectoderm and endoderm (Figures 4B and 4C), as previously reported in the intact animal [25]. However, the epithelial lineages exhibited strikingly different behaviors at tissue boundaries. At the ectodermal wound front, LifeAct-GFP labeled both cell-cell contacts and a protrusive front at fragment edges (Figure 4B'; Video S6), analogous to the actin organization that we observed

at sites of cell internalization in small aggregates (Figure 3A). In contrast, at the endodermal wound front, LifeAct-GFP was no longer enriched at cell-cell contacts but instead diffusely localized in wound-adjacent endodermal cells (Figure 4C'). Additionally, endodermal cells at the wound front exhibited constitutive membrane blebbing (Figure 4C'; Video S6), analogous to that observed in endodermal small aggregates (Figures 2C and S2B). Together, these findings reveal close parallels between cell sorting and wound healing in *Hydra* and raise the possibility that lineage-specific differences in the maintenance and restoration of epithelial organization may factor more broadly into healing and regeneration in the animal.

DISCUSSION

Hydra's ability to self-organize a viable organism from a disordered aggregate of cells provides a unique opportunity to study the mechanisms by which cells establish and maintain positioning to generate precisely patterned, functional tissues. Here, we recapitulated sorting in small aggregates to facilitate high-resolution live imaging and physical manipulation of the process. We found that, following dissociation and reaggregation, ectodermal cells rapidly re-establish epithelial architecture, in contrast to endodermal cells, which remain disordered. The epithelial architecture of the ectoderm restricts cell adhesion to sites of local discontinuity, where non-epithelialized cells are captured. Finally, ectodermal cell spreading restores epithelial continuity, thereby engulfing captured cells and positioning them to the aggregate interior. Based on these findings, we propose a model in which tissue-specific differences in epithelialization drive cell sorting (Figure 5).

Previous investigations of cell sorting in *Hydra* have largely focused on distinguishing two competing models. One frequently evoked model proposes that ectodermal and endodermal cells sort based on their distinct biophysical properties [16, 17]. In support of this model, previous work revealed a higher tissue surface tension in endodermal explants when compared to ectodermal explants, as predicted by common biophysical models of sorting, like the differential adhesion hypothesis and the differential interfacial tension hypothesis [16, 17]. An alternative model ascribes sorting to lineage-specific differences in the rate or direction of cell migration [20, 21]. Broadly, both models emphasize cell-intrinsic differences between endodermal and ectodermal lineages that promote their partitioning to the interior and exterior of a cell aggregate, respectively. Our micromanipulation approach allowed us to directly test the role of cell identity in sorting. We found that ectodermal cells do not intrinsically

(B) Left: schematic of the large aggregate preparation. A suspension of ectodermal and endodermal small aggregates and single cells was pelleted by centrifugation to form large, mixed-lineage aggregates that undergo sorting. Right: representative time course of re-epithelialization in a large aggregate generated from animals expressing ectodermal LifeAct-GFP. Dashed line depicts the boundary of a superficial layer of ectodermal cells spreading and fusing to form a continuous epithelium ($n = 5$ from 4 independent sample preparations).

(C) Left: schematic of aggregate manual assembly from isolated cells using micromanipulation. Right: representative before and after stills of the epithelialization of a manually assembled ectodermal aggregate expressing MRLC-GFP. Acquisition begins after releasing the assembled aggregate from the micropipette ($n = 11$ from 11 independent sample preparations).

(A–C) All frames depict maximum intensity projections of 50-to-100- μm z stacks. See also Video S5 and Figure S4.

(D) Quantification of the number of cells showing epithelial-like morphology and junctional actomyosin localization in manually reassembled ectodermal and endodermal aggregates. Each datapoint represents an individual manually assembled aggregate (ectoderm: $n = 11$ from 11 independent sample preparations; endoderm: $n = 7$ from 7 independent sample preparations). The number of epithelialized cells was scored 60 min after manual reassembly. Timestamps, hh:mm:ss. Scale bars, 20 μm .

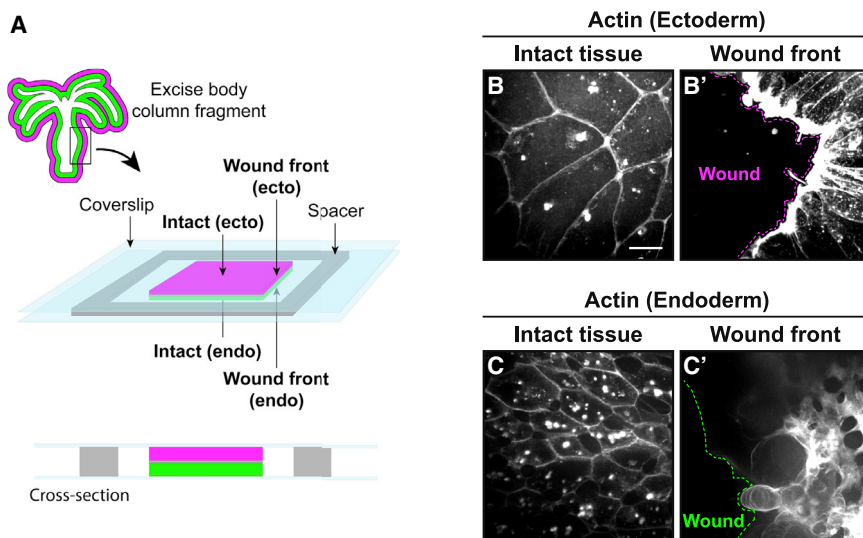


Figure 4. Differential Preservation of Epithelial Architecture Occurs upon Local Wounding

(A) Schematic of wounding assay sample preparation. A living fragment of the body column was excised from the intact animal and sandwiched between coverslips with a 100- μ m spacer. Arrows indicate regions of interest for each tissue and region shown in (B) and (C).

(B) Representative stills from live imaging of dissected body column fragments expressing LifeAct-GFP in the ectoderm. Imaging was performed at the interior (intact, B) and tissue edge (wound front, B') of the same fragment ($n = 3$ from 3 independent sample preparations).

(C) Representative stills from live imaging of dissected body column fragments expressing LifeAct-GFP in the endoderm at the interior (intact, C) and tissue edge (wound front, C') of the same fragment ($n = 3$ from 3 independent sample preparations).

(B and C) Dashed lines indicate the leading edge of the wound front. Intact and wound front images

are scaled differently to improve visualization of features. All frames depict maximum intensity projections of 50-to-100- μ m z stacks. Scale bars, 20 μ m. See also [Video S6](#).

adopt outer positions during sorting in all contexts but can instead adopt inner or outer positions, depending on whether they are presented as single cells or multicellular aggregates (Figures 1C and 1E). This discovery revealed that, to identify the determinants of sorting, the relevant comparison is not (1) ectodermal versus endodermal cells but rather (2) ectodermal aggregates versus single cells of both lineages and endodermal aggregates.

Our data suggest that what distinguishes the ectodermal aggregate from internalized entities is the emergence of a polarized adhesive interface. All internalized entities, including single ectodermal cells and endodermal aggregates, are uniformly adhesive (Figures 1D, 1E, and S1D). In contrast, mature ectodermal aggregates fail to establish stable cell contacts with any cell type placed in contact with their intact apical interfaces (Figures 2A and 2B). This is consistent with prior observations made in larger ectodermal explants, which resist fusion except at freshly cut interfaces [17]. These unique adhesive properties may arise as a result of the ectodermal aggregate's ability to rapidly reconstruct a polarized epithelial monolayer (Figures 3A–3C). One mechanism by which this could occur is through the redistribution of adhesion molecules as polarity is established, as in ectodermal explants of *Xenopus* embryos, in which C-cadherin molecules redistribute exclusively to basolateral membranes and away from free apical interfaces following tissue condensation [33]. Due to the formation of a non-adherent ectodermal surface, cell adhesion is permitted exclusively where the ectodermal epithelium is transiently disrupted (hotspots), and adhered cells are subsequently internalized as these discontinuities are resolved (Figures 2A, 2B, and 3A). These results shed light on previous observations that *Hydra* aggregates transition from homotypic (composed of a single epithelial cell type) to heterotypic (consisting of both ectodermal and endodermal cells) as aggregates expand in size in rotary culture [15]. We speculate that the increase in heterotypic interactions with size may result from an increase in hotspots as aggregate surface area increases.

Our findings support a relatively simple model through which a mixed aggregate can sort if one cell type is predisposed to generate and maintain a polarized monolayer. Under this model, hotspots, which we speculate arise from exposed membranes of the aggregate interior, are returned to the aggregate interior, along with any adhered entities, as ectodermal epithelial continuity and polarity are restored (Figure 5). Intriguingly, this model, arising from our studies in adult *Hydra*, is consistent with frequently overlooked observations from Holtfreter's classic self-organization studies in the amphibian embryo. In particular, he reported that an epithelial sheet of superficial blastomeres (formerly known as the "surface coat") formed an apical barrier to adhesion that promoted its localization to the aggregate exterior in recombined explants [2, 34, 35]. Thus, selective epithelialization may play a role in determining cell positioning during sorting in diverse systems. Interestingly, although this mechanism can account for a bias toward lineage-specific cell sorting, the absence of explicit mechanisms to prevent the internalization of non-epithelialized ectodermal cells may also explain topological defects observed in prior studies of *Hydra* reaggregation, such as the presence of internalized ectodermal compartments that resolve over time [24]. We did not observe internalized cells, including ectodermal cells, re-emerging to the aggregate surface in our experiments, suggesting that sorting error correction may occur over longer timescales or involve alternative mechanisms, such as cell death. Understanding the fate of internalized ectodermal cells and how topological defects within aggregates are resolved is an exciting direction for future study.

We found that the endoderm and ectoderm exhibit differing propensities to maintain and re-establish epithelial organization in a variety of contexts, including after disruption by wounding (Figures 4B and 4C) or dissociation (Figures 2C, 3C, and S4). Importantly, we note that this selective epithelialization may not only restrict polarized adhesion to one lineage, as we describe here for the ectoderm, but likely also influences interfacial tensions and thus may impact sorting in multiple ways. The

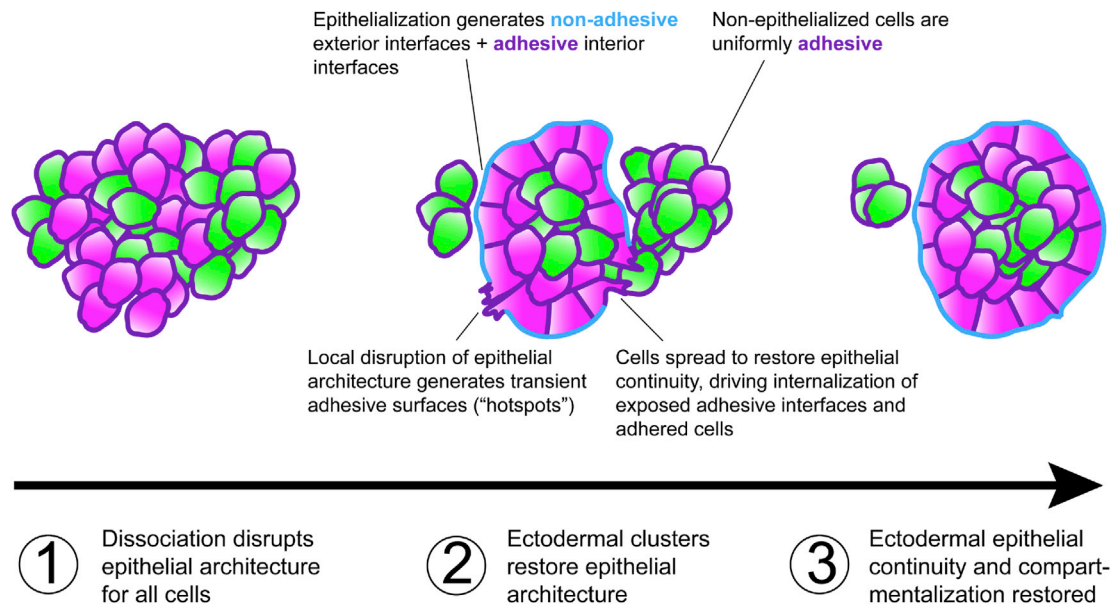


Figure 5. Model of Epithelialization-Mediated Cell Sorting in *Hydra*

Tissue dissociation results in loss of epithelial architecture in both ectodermal and endodermal lineages, rendering them uniformly adherent. Ectodermal aggregates rapidly restore epithelial architecture, generating nonadherent apical surfaces but preserving adherent interior interfaces. Epithelial discontinuities expose adhesive surfaces from the aggregate interior, allowing them to capture adhesive cells. Adhered cells, along with exposed adhesive interfaces, are internalized as ectodermal cells spread to restore epithelial continuity.

mechanisms that underlie these differing propensities for re-epithelialization remain unknown. We did not observe the restoration of epithelial architecture in endodermal aggregates following manual reassembly (Figure S4) or partial dissociation (Figure 2C), even when following these aggregates for several hours. Although the small aggregates used in this study recapitulate the sorting behaviors seen in larger aggregates, small aggregates ultimately dissociate prior to luminogenesis, precluding more prolonged studies of endodermal re-epithelialization, as well as the study of later aspects of the *Hydra* regeneration process. For example, restoration of the extracellular matrix, which normally separates endodermal and ectodermal monolayers, is first observed almost a full day after reaggregation [36], which is beyond the lifetime of our small aggregates. Thus, it is intriguing to consider that endodermal epithelialization may depend on the restoration of the ECM or other features not present in the early stages of regeneration. Together, our data suggest that the capacity to polarize may be intrinsic to the ectoderm, whereas polarization of the endoderm may require inductive cues.

Hydra's capacity to self-assemble an intact animal following complete dissociation raises an intriguing question: how does such a remarkable ability evolve, despite the unlikelihood of such catastrophic tissue damage in nature? We found that differences in the preservation of epithelial architecture also occur during wounding of the *Hydra* body column (Figures 4B and 4C). This raises the possibility that the same mechanisms underlying cell sorting may be broadly elicited for wound healing in *Hydra* and that it may be possible to consider a self-organizing aggregate as a collection of wounds. Notably, the simple sorting mechanism that we describe here facilitates the rapid restoration of ectodermal epithelial integrity, while

simultaneously capturing and internalizing any exposed tissues. It is, therefore, tempting to speculate that induction of an efficient yet simple mechanism for restoring barrier function after wounding may underlie the self-organization of epithelia at the organismal scale in *Hydra*.

STAR★METHODS

Detailed methods are provided in the online version of this paper and include the following:

- KEY RESOURCES TABLE
- RESOURCE AVAILABILITY
 - Lead Contact
 - Materials Availability
 - Data and Code Availability
- EXPERIMENTAL MODEL AND SUBJECT DETAILS
 - *Hydra* culturing and strains
 - Generation of transgenic strains
- METHOD DETAILS
 - Dissociation and reaggregation
 - Microscopy and micromanipulation
 - Drug perturbations
- QUANTIFICATION AND STATISTICAL ANALYSIS

SUPPLEMENTAL INFORMATION

Supplemental Information can be found online at <https://doi.org/10.1016/j.cub.2020.07.035>.

ACKNOWLEDGMENTS

We thank Iain Cheeseman, Celina Juliano, Ophir Klein, Adam Williamson, Rachel Zwick, Jeff Bush, Abby Kindberg, Sophie Dumont, and members of the Vale laboratory for critical discussions and feedback on the manuscript. We are grateful to Celina Juliano and Rob Steele for numerous insights into *Hydra* care and experimentation and, with Bert Hobmayer and Rafael Yuste, for providing *Hydra* lines and reagents. We thank Vasudha Srivastava for critical discussion and training regarding micromanipulation experiments. This material is based upon work supported by the National Science Foundation Graduate Research Fellowship under grant no. 1650113 (to T.D.S.). T.D.S. was also supported by the UCSF Chuan Lyu Discovery Fellowship. R.D.V. was supported by the Howard Hughes Medical Institute. K.L.M. was supported by the Damon Runyon Cancer Research Foundation (DRG-2282-17) and by the Eunice Kennedy Shriver National Institute of Child Health & Human Development of the National Institutes of Health (K99HD101021).

AUTHOR CONTRIBUTIONS

Investigation, Methodology, Validation, Formal Analysis, and Visualization, T.D.S.; Writing – Original Draft, T.D.S. and K.L.M.; Supervision, K.L.M. and R.D.V.; Conceptualization, Writing – Review and Editing, and Funding Acquisition, T.D.S., K.L.M., and R.D.V.

DECLARATION OF INTERESTS

The authors declare no competing interests.

Received: May 12, 2020

Revised: July 5, 2020

Accepted: July 9, 2020

Published: August 13, 2020

REFERENCES

- Lancaster, M.A., and Knoblich, J.A. (2014). Organogenesis in a dish: modeling development and disease using organoid technologies. *Science* **345**, 1247–125.
- Townes, P.L., and Holtfreter, J. (1955). Directed movements and selective adhesion of embryonic amphibian cells. *J. Exp. Zool.* **128**, 53–120.
- Krens, S.F.G., and Heisenberg, C.-P. (2011). Cell sorting in development. *Curr. Top. Dev. Biol.* **95**, 189–213.
- Brodland, G.W. (2002). The differential interfacial tension hypothesis (DITH): a comprehensive theory for the self-rearrangement of embryonic cells and tissues. *J. Biomech. Eng.* **124**, 188–197.
- Foty, R.A., Pflieger, C.M., Forgacs, G., and Steinberg, M.S. (1996). Surface tensions of embryonic tissues predict their mutual envelopment behavior. *Development* **122**, 1611–1620.
- Foty, R.A., and Steinberg, M.S. (2005). The differential adhesion hypothesis: a direct evaluation. *Dev. Biol.* **278**, 255–263.
- Schötz, E.-M., Burdine, R.D., Jülicher, F., Steinberg, M.S., Heisenberg, C.-P., and Foty, R.A. (2008). Quantitative differences in tissue surface tension influence zebrafish germ layer positioning. *HFSP J.* **2**, 42–56.
- Steinberg, M.S. (1962). On the mechanism of tissue reconstruction by dissociated cells. I. Population kinetics, differential adhesiveness, and the absence of directed migration. *Proc. Natl. Acad. Sci. USA* **48**, 1577–1582.
- Steinberg, M.S. (1962). On the mechanism of tissue reconstruction by dissociated cells. III. Free energy relations and the reorganization of fused, heteronomic tissue fragments. *Proc. Natl. Acad. Sci. USA* **48**, 1769–1776.
- Fagotto, F., Rohani, N., Touret, A.-S., and Li, R. (2013). A molecular base for cell sorting at embryonic boundaries: contact inhibition of cadherin adhesion by ephrin/ Eph-dependent contractility. *Dev. Cell* **27**, 72–87.
- Landsberg, K.P., Farhadifar, R., Ranft, J., Umetsu, D., Widmann, T.J., Bittig, T., Said, A., Jülicher, F., and Dahmann, C. (2009). Increased cell bond tension governs cell sorting at the *Drosophila* anteroposterior compartment boundary. *Curr. Biol.* **19**, 1950–1955.
- Monier, B., Pélissier-Monier, A., Brand, A.H., and Sanson, B. (2010). An actomyosin-based barrier inhibits cell mixing at compartmental boundaries in *Drosophila* embryos. *Nat. Cell Biol.* **12**, 60–69.
- Gierer, A., Berking, S., Bode, H., David, C.N., Flick, K., Hansmann, G., Schaller, H., and Trenkner, E. (1972). Regeneration of hydra from reaggregated cells. *Nat. New Biol.* **239**, 98–101.
- Technau, U., and Steele, R.E. (2011). Evolutionary crossroads in developmental biology: Cnidaria. *Development* **138**, 1447–1458.
- Hobmayer, B., Snyder, P., Alt, D., Happel, C.M., and Holstein, T.W. (2001). Quantitative analysis of epithelial cell aggregation in the simple metazoan *Hydra* reveals a switch from homotypic to heterotypic cell interactions. *Cell Tissue Res.* **304**, 147–157.
- Technau, U., and Holstein, T.W. (1992). Cell sorting during the regeneration of *Hydra* from reaggregated cells. *Dev. Biol.* **151**, 117–127.
- Cochet-Escartin, O., Locke, T.T., Shi, W.H., Steele, R.E., and Collins, E.S. (2017). Physical mechanisms driving cell sorting in *Hydra*. *Biophys. J.* **113**, 2827–2841.
- Sato-Maeda, M., Uchida, M., Graner, F., and Tashiro, H. (1994). Quantitative evaluation of tissue-specific cell adhesion at the level of a single cell pair. *Dev. Biol.* **162**, 77–84.
- Takaku, Y., Hariyama, T., Kurachi, M., and Tsukahara, Y. (1999). Ultrastructural observations of adherent cell pairs in *hydra vulgaris*. *J. Exp. Biol.* **202**, 2239–2244.
- Kishimoto, Y., Murate, M., and Sugiyama, T. (1996). *Hydra* regeneration from recombined ectodermal and endodermal tissue. I. Epibolic ectodermal spreading is driven by cell intercalation. *J. Cell Sci.* **109**, 763–772.
- Takaku, Y., Hariyama, T., and Fujisawa, T. (2005). Motility of endodermal epithelial cells plays a major role in reorganizing the two epithelial layers in *Hydra*. *Mech. Dev.* **122**, 109–122.
- Rieu, J.P., Kataoka, N., and Sawada, Y. (1998). Quantitative analysis of cell motion during sorting in two-dimensional aggregates of dissociated *hydra* cells. *Phys. Rev. E* **57**, 924–931.
- Rieu, J.P., Upadhyaya, A., Glazier, J.A., Ouchi, N.B., and Sawada, Y. (2000). Diffusion and deformations of single *hydra* cells in cellular aggregates. *Biophys. J.* **79**, 1903–1914.
- Seybold, A., Salvenmoser, W., and Hobmayer, B. (2016). Sequential development of apical-basal and planar polarities in aggregating epitheliomuscular cells of *Hydra*. *Dev. Biol.* **412**, 148–159.
- Aufschnaiter, R., Wedlich-Söldner, R., Zhang, X., and Hobmayer, B. (2017). Apical and basal epitheliomuscular F-actin dynamics during *Hydra* bud evagination. *Biol. Open* **6**, 1137–1148.
- Holz, O., Apel, D., Steinmetz, P., Lange, E., Hopfenmüller, S., Ohler, K., Sudhop, S., and Hassel, M. (2017). Bud detachment in *hydra* requires activation of fibroblast growth factor receptor and a Rho-ROCK-myosin II signaling pathway to ensure formation of a basal constriction. *Dev. Dyn.* **246**, 502–516.
- Vicente-Manzanares, M., Ma, X., Adelstein, R.S., and Horwitz, A.R. (2009). Non-muscle myosin II takes centre stage in cell adhesion and migration. *Nat. Rev. Mol. Cell Biol.* **10**, 778–790.
- Courtemanche, N., Pollard, T.D., and Chen, Q. (2016). Avoiding artefacts when counting polymerized actin in live cells with LifeAct fused to fluorescent proteins. *Nat. Cell Biol.* **18**, 676–683.
- Flores, L.R., Keeling, M.C., Zhang, X., Sliogeryte, K., and Gavara, N. (2019). Author correction: Lifeact-TagGFP2 alters F-actin organization, cellular morphology and biophysical behaviour. *Sci. Rep.* **9**, 9507.
- Paluch, E., Piel, M., Prost, J., Bornens, M., and Sykes, C. (2005). Cortical actomyosin breakage triggers shape oscillations in cells and cell fragments. *Biophys. J.* **89**, 724–733.
- Bement, W.M., Forscher, P., and Mooseker, M.S. (1993). A novel cytoskeletal structure involved in purse string wound closure and cell polarity maintenance. *J. Cell Biol.* **121**, 565–578.

32. Nusrat, A., Delp, C., and Madara, J.L. (1992). Intestinal epithelial restitution. Characterization of a cell culture model and mapping of cytoskeletal elements in migrating cells. *J. Clin. Invest.* **89**, 1501–1511.
33. Luu, O., David, R., Ninomiya, H., and Winklbauer, R. (2011). Large-scale mechanical properties of *Xenopus* embryonic epithelium. *Proc. Natl. Acad. Sci. USA* **108**, 4000–4005.
34. Holtfreter, J. (1944). A study of the mechanics of gastrulation. Part II. *J. Exp. Zool.* **95**, 171–212.
35. Holtfreter, J. (1943). Properties and functions of the surface coat in amphibian embryos. *J. Exp. Zool.* **93**, 251–323.
36. Sarras, M.P., Jr., Zhang, X., Huff, J.K., Accavitti, M.A., St John, P.L., and Abrahamson, D.R. (1993). Extracellular matrix (mesoglea) of *Hydra vulgaris* III. Formation and function during morphogenesis of hydra cell aggregates. *Dev. Biol.* **157**, 383–398.
37. Glauber, K.M., Dana, C.E., Park, S.S., Colby, D.A., Noro, Y., Fujisawa, T., Chamberlin, A.R., and Steele, R.E. (2013). A small molecule screen identifies a novel compound that induces a homeotic transformation in *Hydra*. *Development* **140**, 4788–4796.
38. Hemmrich, G., Khalturin, K., Boehm, A.-M., Puchert, M., Anton-Erxleben, F., Wittlieb, J., Klostermeier, U.C., Rosenstiel, P., Oberg, H.-H., Domazet-Lošo, T., et al. (2012). Molecular signatures of the three stem cell lineages in *hydra* and the emergence of stem cell function at the base of multicellularity. *Mol. Biol. Evol.* **29**, 3267–3280.
39. Siebert, S., Farrell, J.A., Cazet, J.F., Abeykoon, Y., Primack, A.S., Schnitzler, C.E., and Juliano, C.E. (2019). Stem cell differentiation trajectories in *Hydra* resolved at single-cell resolution. *Science* **365**, eaav9314.
40. Stuurman, N., Edelstein, A.D., Amodaj, N., Hoover, K.H., and Vale, R.D. (2010). Computer control of microscopes using μ Manager. *Curr. Protoc. Mol. Biol.* *Chapter 14*, Unit 14.20.
41. Juliano, C.E., Lin, H., and Steele, R.E. (2014). Generation of transgenic *Hydra* by embryo microinjection. *J. Vis. Exp.* 51888.
42. Wittlieb, J., Khalturin, K., Lohmann, J.U., Anton-Erxleben, F., and Bosch, T.C.G. (2006). Transgenic *Hydra* allow in vivo tracking of individual stem cells during morphogenesis. *Proc. Natl. Acad. Sci. USA* **103**, 6208–6211.
43. UniProt Consortium (2019). UniProt: a worldwide hub of protein knowledge. *Nucleic Acids Res.* **47** (D1), D506–D515.
44. Lenhoff, H. (2013). *Hydra: Research Methods* (Springer Science & Business Media).

STAR★METHODS

KEY RESOURCES TABLE

| REAGENT or RESOURCE | SOURCE | IDENTIFIER |
|----------------------------------------------------------------------------------|-------------------------------------------------------------------------|-------------------|
| Biological Samples | | |
| <i>Hydra vulgaris</i> cDNA | Celina Juliano, UC Davis | N/A |
| Chemicals, Peptides, and Recombinant Proteins | | |
| (S)-nitro-Blebbistatin | Cayman Chemical | Cat#13891 |
| CaCl ₂ ·2H ₂ O | Sigma-Aldrich | SKU: C5080 |
| MgSO ₄ ·7H ₂ O | Sigma-Aldrich | SKU: M1880 |
| KCl | Sigma-Aldrich | SKU: P3911 |
| HEPES, sodium salt | Research Products International | SKU: H75050 |
| Na ₂ HPO ₄ ·2H ₂ O | Sigma-Aldrich | SKU: 71643 |
| KH ₂ PO ₄ | Sigma-Aldrich | SKU: P9791 |
| Na Pyruvate | Sigma-Aldrich | SKU: P5280 |
| Na ₃ Citrate·2H ₂ O | Sigma-Aldrich | SKU: C8532 |
| Rifampicin | Sigma-Aldrich | SKU: R3501 |
| Deposited Data | | |
| EB1 predicted homolog | Juliano aepLRv2, <i>Hydra</i> 2.0 Genome Project Portal, NHGRI, NIH | t4232aep |
| MRLC predicted homolog | Juliano aepLRv2, <i>Hydra</i> 2.0 Genome Project Portal, NHGRI, NIH | t34427aep |
| Experimental Models: Organisms/Strains | | |
| <i>Hydra vulgaris</i> : DsRed2(ectoderm)/GFP(endoderm), “Inverse Watermelon” | Celina Juliano, UC Davis [37]; | N/A |
| <i>Hydra vulgaris</i> : GFP(ectoderm)/DsRed2(endoderm), “Watermelon” | Rob Steele, UC Irvine [37]; | N/A |
| <i>Hydra vulgaris</i> : LifeAct-GFP(ectoderm) | Bert Hobmayer, University of Innsbruck [25]; | N/A |
| <i>Hydra vulgaris</i> : LifeAct-GFP(endoderm) | Bert Hobmayer, University of Innsbruck [25]; | N/A |
| <i>Hydra vulgaris</i> : GFP(interstitial stem cell): pCnno1::eGFP | Celina Juliano, UC Davis [38]; | N/A |
| <i>Hydra vulgaris</i> : GFP(neuron), “nGreen”: pActin::GFP(interstitial lineage) | Rob Steele, UC Irvine [39]; | N/A |
| <i>Hydra vulgaris</i> : pActin::EB1-GFP(interstitial lineage) | This manuscript | N/A |
| <i>Hydra vulgaris</i> : pActin::MRLC-GFP(ectoderm) | This manuscript. | N/A |
| <i>Hydra vulgaris</i> : AEP SS1 | Rob Steele, UC Irvine | N/A |
| Oligonucleotides | | |
| EB1 Forward: ATGGCAGTAAATGTTTTTAA TACTGGTGTC | Integrated DNA Technologies | N/A |
| EB1 Reverse: ATATTCATCAGCCTCTCCAGA AATTTCTTCTC | Integrated DNA Technologies | N/A |
| MRLC Forward: ATGTCTTCGAGTAAGAAAAC CAAGAAGGG | Integrated DNA Technologies | N/A |
| MRLC Reverse: TTCCTCTTGGATCCGTGTTT AATGATTC | Integrated DNA Technologies | N/A |
| Recombinant DNA | | |
| pHyVec4 | Rob Steele, UC Irvine | Addgene ID: 34791 |
| phTS4: plasmid encoding MRLC-GFP | This manuscript | N/A |
| phTS5: plasmid encoding EB1-GFP | This manuscript | N/A |
| Software and Algorithms | | |
| Micro-Manager v.2.0 | https://micro-manager.org [40]; | N/A |

RESOURCE AVAILABILITY

Lead Contact

Further information and requests for resources and reagents should be directed to and will be fulfilled by the Lead Contact, Ronald D. Vale (valer@janelia.hhmi.org).

Materials Availability

Materials generated in this study, including plasmids encoding EB1-GFP and MRLC-GFP, and transgenic *Hydra* expressing MRLC-GFP(ectoderm), are available upon request. The transgenic *Hydra* strain expressing MRLC-GFP(nematocyte) was lost during the course of this study and is, therefore, no longer available.

Data and Code Availability

No unique code was generated during this study. Source data are available upon request.

EXPERIMENTAL MODEL AND SUBJECT DETAILS

Hydra culturing and strains

Hydra were maintained at 18°C and fed 2-3 times per week with *Artemia* nauplii (Brine Shrimp Direct). Animals were fed ≥ 24 h prior to dissociation or imaging. Non-budding animals were chosen for experimentation. The following transgenic lines were used for re-gregation and internalization experiments:

DsRed2(ectoderm)/GFP(endoderm) [37]
GFP(ectoderm)/DsRed2(endoderm) [37]
LifeAct-GFP(ectoderm) [25]
LifeAct-GFP(endoderm) [25]
pCnnos1::eGFP (interstitial stem cell reporter) [38]
pActin::GFP(interstitial lineage) (“nGreen,” neuronal reporter) [39]
AEP SS1 (courtesy of Rob Steele)
pActin::EB1-GFP(interstitial lineage) (this manuscript)
pActin::MRLC-GFP(ectoderm) (this manuscript)

Generation of transgenic strains

New transgenic *Hydra* strains were generated as described [41, 42]. Predicted homologs of EB1 (t4232aep) and MRLC (t34427aep) were identified by comparing known sequences obtained from UniProt [43] against the *Hydra* 2.0 Genome Project and Juliano aepLRv2 nucleotide databases (<https://research.nhgri.nih.gov/hydra/>) using BLAST (<https://blast.ncbi.nlm.nih.gov>). Coding sequences were cloned from *Hydra* cDNA using primers containing the following sequences:

EB1 Forward: ATGGCAGTAAATGTTTTAATACTGGTGTC
EB1 Reverse: ATATTCATCAGCCTCTCCAGAAATTTCTTCTC
MRLC Forward: ATGTCTTCGAGTAAGAAAACCAAGAAGGG
MRLC Reverse: TTCCTCTTTGGATCCGTGTTAATGATTC

Coding sequences were subcloned into expression vector pHyVec4 (Addgene ID 34791), between Nhe1 and Xma1 restriction enzyme sites. The resulting plasmids (pHTS4, pHTS5) were injected into 1-4-cell-stage *Hydra* embryos of the AEP SS1 strain using a FemtoJet 4i microinjector (Eppendorf), TransferMan 4r micromanipulator (Eppendorf), and dissecting microscope.

METHOD DETAILS

Dissociation and re-agggregation

Dissociation and re-agggregation were performed broadly as described [24, 44], with some modifications. In brief, ~ 10 -30 animals were incubated at 4°C for 30-60 min in a filter-sterilized hyperosmotic Dissociation Medium (DM) pH 6.9-7.0: CaCl₂·2H₂O (5 mM), MgSO₄·7H₂O (1 mM), KCl (2.8 mM), HEPES (11 mM), Na₂HPO₄ (0.67 mM), KH₂PO₄ (0.44 mM), Na Pyruvate (5 mM), Na₃ Citrate·2H₂O (5 mM), Rifampicin (50 μ g/mL). Animals were then dissociated by shear stress by passing through the opening of a glass pipette against the bottom of a 1.5-mL microcentrifuge tube. Animals were sheared in two rounds, first by pipetting ~ 10 times and discarding the supernatant, adding fresh 4°C DM, then pipetting ~ 20 -30 times to generate the final cell suspension. After incubating the tube on ice for ~ 1 min to allow large tissue fragments to settle out of suspension, the supernatant containing single cells and small aggregates was collected. Internalization and adhesion experiments were performed within 3 h of dissociation of a given sample. For internalization assays, single cells and small aggregates of particular cell types were identified by cell type- or lineage-specific fluorescence

reporters, isolated by pipette, transferred to imaging chambers, and positioned using the micropipette aspirator (described below). Notably, small aggregates consisted of a single epithelial cell type but maintained some interactions with cells of the interstitial lineage, which are non-fluorescent but can be detected by nuclear staining. To generate large mixed-lineage aggregates, cell suspensions were divided into 150-to-300- μ L volumes (depending on desired aggregate size) and centrifuged at 800 x g for 6 min to pellet. Pelleted samples were incubated on ice for \sim 5 min to allow aggregates to detach from the tube wall, and aggregates were collected by pipette and transferred to imaging chambers or coverslips.

Microscopy and micromanipulation

Images were acquired on a Yokogawa CSU-X spinning disk confocal attached to an inverted Nikon Ti-E microscope, and Andor iXon Ultra 897 EM-CCD camera (Figures 2C and S2B single cell ectodermal panel), or a Yokogawa CSU100 spinning disk confocal attached to an inverted Nikon Ti-E microscope, a Hamamatsu C9100-13 EMCCD camera (all other images), all using Micro-Manager software [40]. Z stacks were acquired at 2-to-10- μ m step sizes for a total depth of 50-100 μ m, at 15-, 30-, or 60-s time intervals, except where higher z-resolution was desired. For higher z-resolution, stacks were acquired at 0.2-to-1- μ m step sizes. All z stacks were acquired with a 60XA 1.20 NA Plan Apo water immersion objective, with the exception of Figure S1A, which was acquired with a 20X Plan Apo VC objective. Maximum intensity projections of 50-to-100- μ m Z stacks are shown throughout, unless otherwise specified.

Imaging chambers were custom assembled from laser cut, rectangular acrylic frames to which coverslips were adhered with vacuum grease (Dow Corning). Micromanipulation experiments used a suction pipette mounted to a Narishige motor-driven micro-manipulator (MM-94) via Narishige microscope mounting adaptor, injection holder, and universal joint (NN-H-4, HI-9, UT-2, respectively). Pipettes were pulled from Sutter Instrument capillary tubes (#B150-110-10) on a Sutter Instrument micropipette puller (P-1000). To achieve the desired opening diameter of 5-10 μ m, pulled pipettes were forged on a microforge (MicroData Instruments, Inc. MFG-3). Suction was controlled by adjusting the elevation of a water column or syringe attached to the suction pipette. Single cells of a particular cell type were brought into contact and held until adhesion occurred and then released. Where necessary, LifeAct-GFP-expressing ectodermal cells were distinguished from GFP-expressing endodermal cells by the cell-cortex specific localization of LifeAct-GFP, and the natural pigmentation of endodermal cells visible by transmitted light. To minimize cell sticking for internalization experiments involving interstitial lineage cell types, coverslips were passivated prior to experimentation by incubation for 1 h in 5% Hellmanex III (Hellma) heated to boiling then maintained at 50°C. Following Hellmanex treatment, coverslips were washed 10 times in deionized water, blocked for 1 h in 4% bovine serum albumin at room temperature, and washed to remove excess BSA.

Drug perturbations

(S)-nitro-Blebbistatin (Cayman Chemical, Cat #13891) stock solution was prepared in DMSO and diluted directly into imaging chamber dissociation medium to a final concentration of 2.5 μ M during or immediately preceding acquisition.

QUANTIFICATION AND STATISTICAL ANALYSIS

Measurements of aggregate sizes were performed in FIJI using the built-in measure function for a line segment drawn along the long axis of aggregates. Measures reflect aggregates that were isolated following small aggregate preparation and do not reflect the complete size distributions for entities found in suspensions, which also contain small cell clusters, single cells, and debris. Successful internalization, as quantified in Figures 1 and S1 (figure legend), was defined as the complete envelopment of an isolated cell within 1 h after cells adhered to pre-identified hotspots. Successful adhesion, as quantified in Figure 2, was defined by persistent, unassisted contact between aggregates and isolated cells and their coordinated movement when manipulated by pipette. Aggregates and cells were continuously repositioned to maintain contact for at least 15 min or until adhesion occurred, whichever arose first. "Epithelialized" cells, as quantified in Figure 3, were defined by the adoption of a flattened and persistent morphology, lack of blebbing, and local enrichment of actin or myosin at cell junctions. Unless noted, all other images/videos are representative of observations made over all replicates specified in figure legends. Independent preparations specified in figure legends indicate completely independent dissociations and aggregate isolations performed on healthy animals.

Current Biology, Volume 30

Supplemental Information

Cell Sorting in *Hydra vulgaris*

Arises from Differing Capacities

for Epithelialization between Cell Types

Taylor D. Skokan, Ronald D. Vale, and Kara L. McKinley

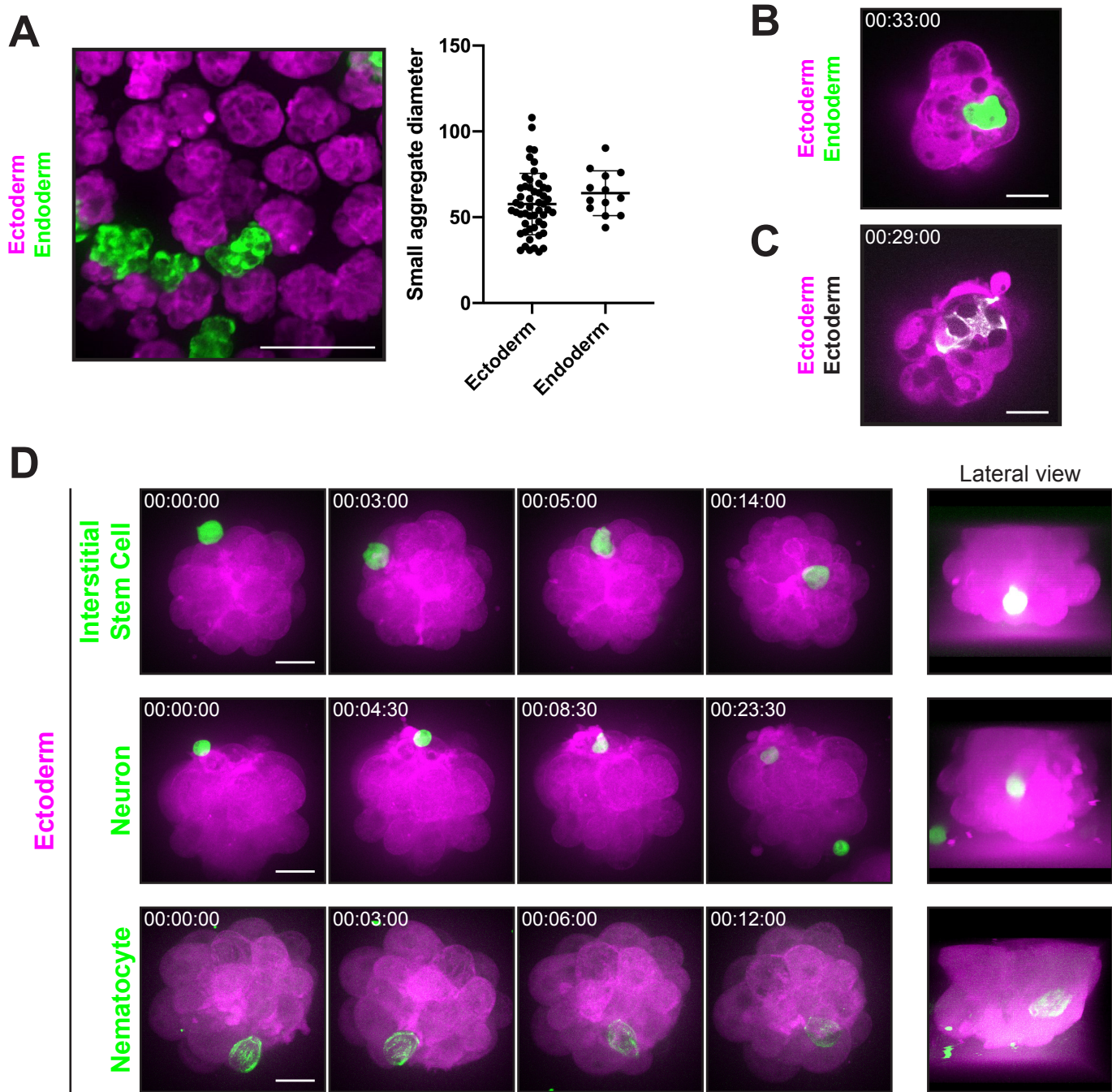


Figure S1. Ectodermal aggregates internalize diverse Hydra cell types, Related to Figure 1. A) Left: Field of view depicting small aggregates isolated via dissociation protocol. Ectodermal aggregates express DsRed2 (magenta). Endodermal aggregates express GFP (green). Right: Quantification of ectodermal and endodermal aggregate diameters (mean \pm s.d., $n = 53$ ectoderm from 7 independent preparations, 13 endoderm from 9 independent preparations). Scalebar, 100 μm . B) Optical section of the final timepoint in Figure 1C, depicting a DsRed2-expressing ectodermal aggregate (magenta) after internalizing a GFP-expressing endodermal cell (green). Section corresponds to a single z-slice at a depth of 21 μm from the aggregate surface. C) Optical section of the final timepoint in Figure 1E, depicting a DsRed2-expressing ectodermal aggregate (magenta) after internalizing a LifeAct-GFP-expressing ectodermal cell (white). Section corresponds to a single z-slice at a depth of 16 μm from the aggregate surface. D) Representative time-courses of ectodermal aggregates expressing DsRed2 (magenta) internalizing isolated cells of the interstitial cell lineage (green). Top: interstitial stem cells expressing GFP ($n = 7/12$ internalized from 7 independent sample preparations); middle: neurons expressing GFP ($n = 5/5$ internalized from 3 independent sample preparations); bottom: nematocytes expressing EB1-GFP ($n = 2/2$ internalized from 2 independent sample preparations). Lateral views were generated from 3D reconstructions of high-resolution z-stacks recorded after the respective time courses and optically rotated for visualization in the Y-Z plane. For these experiments, coverslips were passivated by Hellmanex III treatment followed by BSA blocking to prevent cell sticking. See also Video S1. (B-D) Scalebars, 20 μm . (A-D) Unless specified, all frames depict maximum intensity projections of 50-100 μm z-stacks. Timestamps, hh:mm:ss.

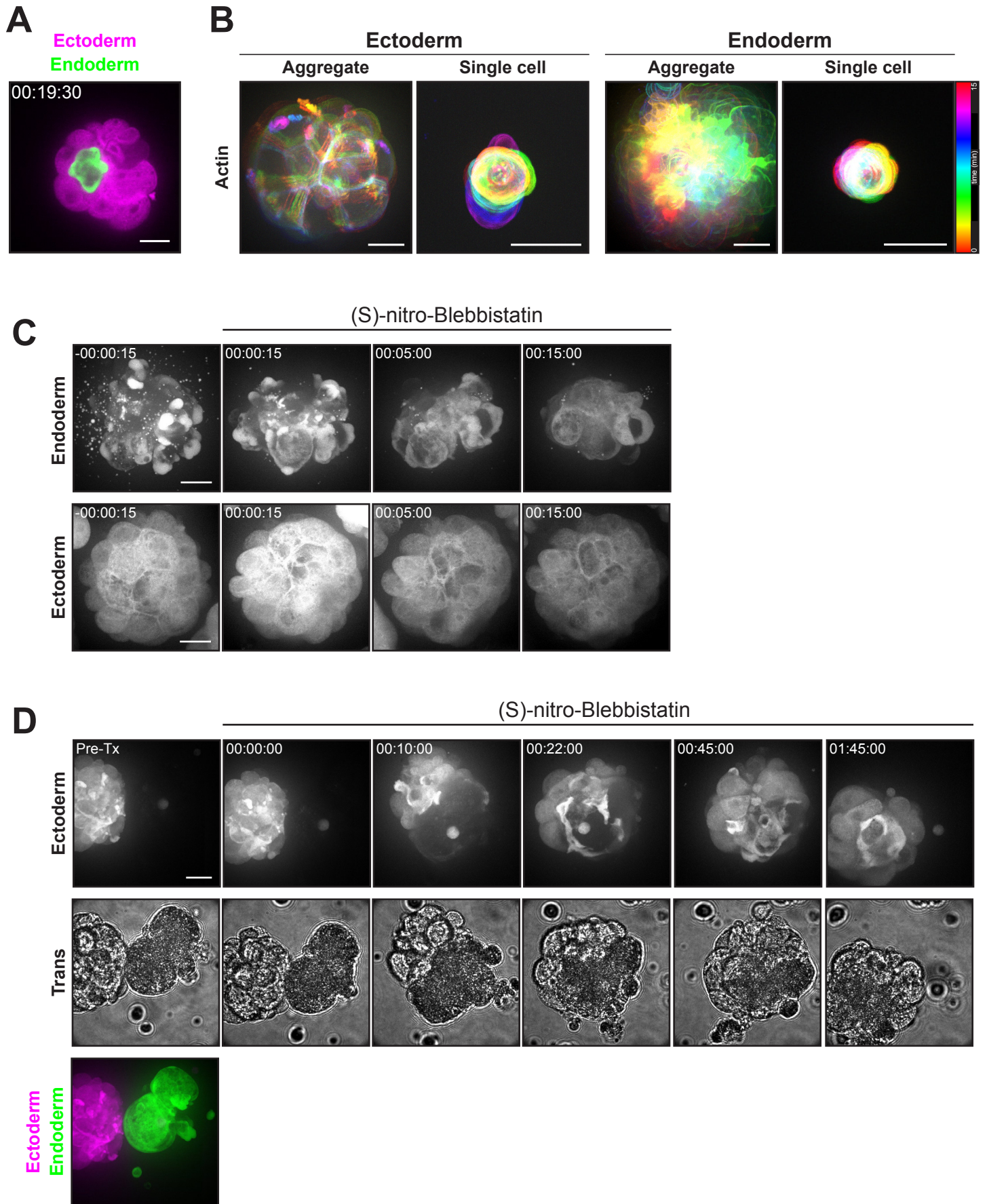


Figure S2. Endodermal blebbing is not essential for internalization, Related to Figure 2. A) Optical section of the final timepoint in Figure 2A (bottom), depicting a DsRed2-expressing ectodermal aggregate (magenta) after internalizing a GFP-expressing endodermal cell (green). Section corresponds to a single z-slice at a depth of 21 μ m from the... (Cont'd)

(Figure S2 cont'd) aggregate surface. B) Temporal color-coded time-series depicting the actin organization and dynamics of the aggregates and single cells shown in Figure 2C. Images were recorded at 15 s time points. See also Video S2. C) Representative time-courses of endodermal or ectodermal aggregates treated with 2.5 μ M (S)-nitro-Blebbistatin. Aggregates express DsRed2. Time stamp indicates time relative to drug addition. (S)-nitro-Blebbistatin inhibits blebbing in endodermal aggregates, with no observable effect on ectodermal aggregates (n = 4 from 4 independent sample preparations). D) Representative time-course of an ectodermal aggregate expressing DsRed2 internalizing an endodermal aggregate expressing GFP in the presence of 2.5 μ M S-Nitro-Blebbistatin. Acquisition began immediately after drug addition. Due to the photoreactivity of S-Nitro-Blebbistatin with blue light, the endoderm (expressing GFP) cannot be imaged after drug addition. Therefore, the endodermal aggregate's position was assessed using transmitted light (trans). A single fluorescent z-stack was taken in both channels before treatment (Pre-Tx) to confirm the identity of aggregates (bottom; ectoderm, magenta; endoderm, green) (n = 10 from 10 independent sample preparations). (B-C) See also Video S3. (B-D) All fluorescence channel frames depict maximum intensity projections of 50-100 μ m z-stacks. Transmitted light channel frames depict single z-sections. Timestamps, hh:mm:ss. Scalebars, 20 μ m.

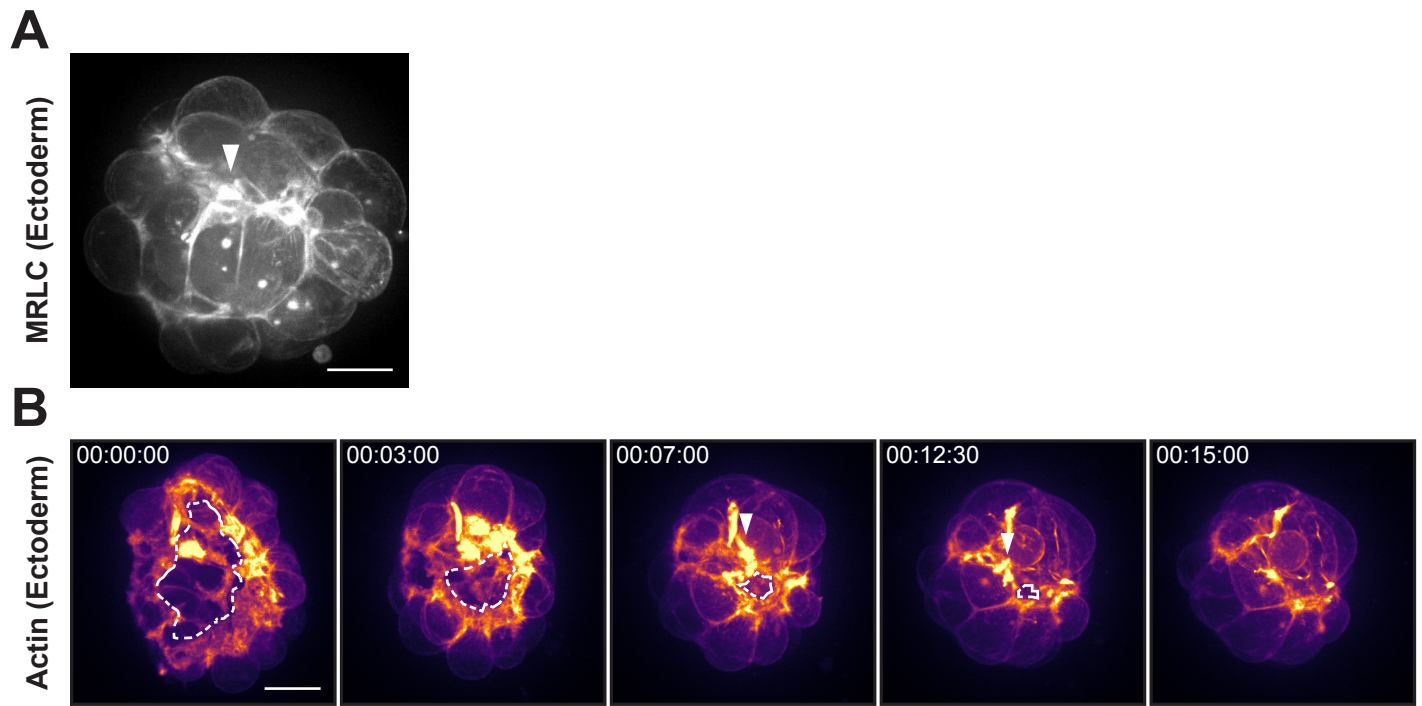


Figure S3. Hotspots emerge at sites of epithelial remodeling, Related to Figure 2. A) Representative still of an ectodermal aggregate expressing MRLC-GFP. Arrowhead indicates hotspot ($n = 10$ from 10 independent sample preparations). B) Representative time-course of an ectodermal tissue fragment expressing LifeAct-GFP rounding into a spherical aggregate immediately after dissociation. Mpl-inferno LUT (FIJI) was applied to aid in visualizing graded LifeAct-GFP signal. Dashed line indicates fragment edges. Arrowhead denotes a hotspot forming where fragment edges met to establish new cell contacts ($n = 7$ from 6 independent sample preparations). See also Video S4. (A-B) All frames depict maximum intensity projections of 50-100 μm z-stacks. Timestamps, hh:mm:ss. Scalebars, 20 μm .

Actin (Endoderm)

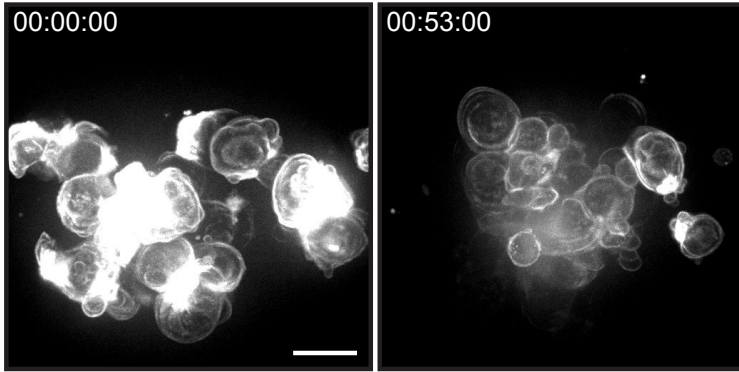


Figure S4. Manually assembled endodermal aggregates fail to restore epithelial architecture, Related to Figure 3. Representative before and after stills of a manually assembled endodermal aggregate expressing LifeAct-GFP. No signs of epithelialization were observed ($n = 7$ from 7 independent sample preparations; see additional quantification in Figure 3D). Acquisition began after releasing the assembled aggregate from the micropipette. All frames depict maximum intensity projections of 50-100 μm z-stacks. Timestamps, hh:mm:ss. Scalebars, 20 μm . See also Video S5.